Effects of Deformation Behavior and Processing Temperature on the Fatigue Performance of Deep-Rolled Medium Carbon Bar Steels

M.D. RICHARDS, M.E. BURNETT, J.G. SPEER, and D.K. MATLOCK

The effects of processing temperature on the deep-rolling response of three medium carbon bar steels, a quenched and tempered 4140 alloy, a 0.34C, 1.21Mn, 0.66Si nontraditional bainitic alloy, and a 0.36C, 1.37Mn V-microalloyed ferrite plus pearlite steel, was assessed through bending fatigue. The significantly different deformation behaviors of the three alloys were characterized through standard and nonstandard quasi-static and cyclic uniaxial tension and compression tests at room temperature (RT) and *in situ* at temperatures up to 634 K. Deep rolling, performed at RT and at elevated temperature (HT) in the dynamic strain-aging (DSA) regime, increased measured endurance limits by 51-62 pct (RT) and 96-117 pct (HT) as compared with the baseline condition. The enhanced fatigue performance by RT deep rolling primarily reflected the effects of the introduction of favorable residual stresses. The improved fatigue performance from HT deep rolling was attributed to the enhanced resistance to strain reversal of the material deformed during deep rolling, due to a change in deformation mechanism from dislocation-interstitial interactions in the DSA regime during processing, which inhibited mechanically induced relaxation of residual stress during cyclic loading.

DOI: 10.1007/s11661-012-1371-6

I. INTRODUCTION

STRUCTURAL and power transfer components used in automotive and heavy equipment applications require materials that exhibit high fatigue resistance. Crankshafts, which are typically manufactured from steel or cast iron, require processing to improve the resistance to bending fatigue at fillets and other highly stressed locations. In comparison to cast iron, steel forgings offer greater strength and durability, improved noise suppression, and lower reciprocating mass, which enable high performance, fuel-efficient engines.[1] Common processes to improve the fatigue performance in crankshafts include shot peening, induction hardening, and deep rolling. Deep rolling has gained industrial interest because of its ability to provide substantial improvement in fatigue performance and offer cost advantages compared with shot peening.[2–4]

Deep rolling is an axially symmetric deformation process for components with a circular cross section, in which a hardened profiled roller is pressed into a machined fillet inducing localized plastic deformation, while the workpiece is rotated.[2,3] The deformation burnishes the surface and introduces nonuniform plastic strain into the fillet cross section[2] which results in a strain hardened surface layer with substantial compressive residual stress. Fatigue performance is increased through an improvement in surface finish, work hardening of the surface material, and the introduction of compressive residual stress at the surface.[2,3] Parameters for the deep-rolling process are the applied force during deep rolling, the number of passes under load by the profiled roller on the workpiece (*i.e.*, ''over-rollings''), rolling speed, lubrication, roller surface finish, and rolling profile.[2] Deformation induced during deep rolling is a result of the stress profile generated from contact between a roller and the workpiece and depends on the material properties and geometry of the two bodies. For a constant number of over-rollings, with an increase in applied rolling force, the fatigue performance increases to a maximum, beyond which a further increase in force degrades fatigue performance.[5–12] The change in fatigue performance indicates that the magnitude and distribution of the induced residual stress field can be modified by a change in the deep-rolling processing parameters.

Development of compressive residual stress occurs in opposition of the plastic strain developed during deep rolling, and is considered to be the most influential factor which leads to improvement in fatigue performance in deep-rolled components.[9,13] Superposition of the residual compressive stress and the tensile component of the imposed bending stress will reduce the maximum tensile stress at the surface during cyclic loading, which will increase the fatigue performance in cyclically loaded components. However, superposition

M.D. RICHARDS, formerly with the Advanced Steel Processing and Products Research Center, Colorado School of Mines, Golden, CO 80401, is now Research Metallurgist at Evraz, Pueblo, CO 81004. Contact e-mail: mdrichar@gmail.com J.G. SPEER and D.K. MATLOCK, Professors, are with the Advanced Steel Processing and Products Research Center, Colorado School of Mines. M.E. BURNETT, Technologist, is with The Timken Co., Canton, OH 44706.

Manuscript submitted July 15, 2011.
Article published online September 22, 2012

of the compressive residual stress and imposed compressive bending stress also has the capacity to generate large compressive stresses during cyclic loading. If the resultant stress exceeds the local flow stress in the direction opposite to that of the deformation generated during deep rolling, then plastic deformation will occur and may relax the residual stress.[9,14,15] For example, Galzy *et al.*[14] demonstrated in a deep-rolled steel crankshaft during loading that the combined effect of the compressive residual stress and the compressive bending stress was sufficient to induce plastic strain in deep-rolled fillets leading to a change from compression to tension residual stress at the surface of the crankshaft fillet.

The stability of residual stress introduced through plastic deformation is limited by the ability of a material to resist deformation during a strain reversal. Resistance to strain reversal is a measure of the susceptibility to the Bauschinger effect,[16] which is a manifestation of nonisotropic hardening during plastic deformation in an isotropic material.[17] In polycrystalline materials, the Bauschinger effect is typified by a loss of the distinct transition between elastic and plastic deformations during strain reversal in addition to a substantial loss of resistance to flow in the reversed direction as compared with the point of strain reversal. The Bauschinger effect has been attributed to large numbers of dislocations moving in a reverse direction during a strain reversal,[18] a process attributed to short-[19–22] and long-[19–23] range effects. Variations in the directionality of short-range dislocation motion have been attributed to reductions in dislocation energy associated with the recovery of "dislocation debris" such as jogs and kinks[21] with reversed dislocation motion. Long-range effects are attributed to microstructural scale internal stresses that assist dislocation motion in the reverse direction. Development of internal stresses has been attributed to dislocation pile-ups at impermeable barriers such as grain boundaries, the walls of cellular dislocation structures, and Orowan loops around strong second-phase particles.[19–22,24–31]

Further enhancements in fatigue strength *via* processing by mechanical deformation processes, such as deep rolling[32,33] can be realized by improving the stability of engineered residual stresses through controlling the resistance of a material to strain reversal by alloying or processing to minimize the Bauschinger effect. Enhanced resistance to the Bauschinger effect can be realized by stabilizing dislocation structures developed during processing. Possible processing methodologies to stabilize dislocation structures include aging of deformed microstructures as is done in the production of low-relaxation cold-drawn wires[34] or deformation of materials at temperatures in the dynamic strain aging (DSA) range where the combined effects of the interaction energy between dislocations and solute atmospheres and the increased solute mobility induce a change in deformation mechanism which is characterized by rapid and repeated pinning and generation of dislocations.[26,35] Examples of these processes are the shot peening of AISI 4140 alloy steel at elevated temperature (HT)[36,37] and the HT deep rolling of SAE 1045 plain carbon steel,[38–40] 304 austenitic stainless steel,[41] and an Al-Mg-Si-Cu alloy.[42]

The results of the change in deformation mechanisms are a decrease in mobile dislocations through solute pinning, an increase in dislocation density,[35,43,44] and a change from cellular dislocation structures to diffuse dislocation tangles.[44–46] For example, Li *et al.*[47] in their analysis of low carbon steels showed that the reversed flow behavior of specimens pre-strained at DSA temperatures exhibited a significant improvement in yield strength and return of a sharp yield point in comparison with specimens pre-strained at room temperature (RT). Richards *et al.*[48] have shown that the Bauschinger effect, as quantified by 0.2 pct offset flow stress measurements after the point of strain reversal, was minimized at the temperature corresponding to peak DSA in a series of single reversal Bauschinger effect tests in medium carbon bar steels. The improved resistance to strain reversal was attributed to the change in deformation mechanism achieved during DSA resulting in a diffuse dislocation structure, which reduced long-range oriented backstresses, reduced dislocation mobility due to solute pinning, and increased dislocation density.

In this article, the potential to utilize mechanical processing at DSA temperatures to stabilize dislocation structures developed during deep rolling was evaluated with three medium carbon forging steels selected to exhibit significantly different strain hardening behaviors. Selected nontraditional mechanical tests were used to provide an improved understanding of the fatigue performance gains realized by deep rolling.

II. EXPERIMENTAL PROCEDURES

Three commercially produced medium carbon forging steels were selected to represent microstructural classes resulting from differences in alloying and thermomechanical processing, and thus exhibit a wide range of strain hardening behaviors. The steels included a quenched and tempered 4140 steel, a nontraditional bainitic (NTB) steel, and a microalloyed ferrite-pearlite steel (C38M) with compositions as summarized in Table I.

The 4140 alloy, received as 32-mm-diameter heat-treated bar which was air cooled after hot rolling, was induction heated to an austenitizing temperature of 1122 K (849 °C), quenched, induction tempered at 1033 K (760 °C) for less than 1 minute, and subsequently air cooled to produce a final hardness of 30 HRC. The NTB was made of a 28.5-mm-diameter NTB steel in which the traditional bainitic carbide morphology was replaced with aggregates of martensite plus retained austenite (MA).[49] The NTB alloy was direct cooled from hot-rolling temperatures to RT. The presence of 0.66 wt pct silicon retarded cementite formation on cooling below the eutectoid temperature due the insolubility of silicon in cementite. Based on X-ray diffraction (XRD) analysis,[50] the NTB steel contained 14.5 pct retained austenite with 1.63 wt pct carbon in the austenite. The NTB alloy had an as-received

Table I. Chemical Compositions of the Steels (Weight Percentage)

Steel	C	Mn	S	Si	Ni	Cr
4140	0.41	0.82	0.039	0.09	0.08	0.89
NTB	0.34	1.21	0.008	0.66	0.10	0.10
C38M	0.36	1.37	0.069	0.56	0.07	0.13
Steel	Mo	V	Nb	Al	Ti	N
4140	0.18	0.001	0.001	0.030	0.010	0.008
NTB	0.19	0.090	0.001	0.010	0.020	0.010
C38M	0.02	0.100	0.010	0.030	0.010	0.016

hardness of 25 HRC. The C38M was a microalloyed and sulfur-modified 1038 steel, commonly used for forged crankshafts, with a ferrite-pearlite microstructure resulting from hot rolling followed by air cooling to produce a hardness of 25 HRC in the as-received 127-mm diameter bar.

Mechanical properties of the as-received alloys were evaluated with uniaxial tension and compression tests at RT at a constant engineering strain rate of 1.6×10^{-3} seconds^{-1}. The resistance to strain reversal and susceptibility to the Bauschinger effect were characterized through *in situ* single reversal, tension to compression tests at a tensile plastic pre-strain level of 0.02 and a constant engineering strain rate of 10^{-4} seconds^{-1} between RT and 634 K (361 °C).[48] Responses of the three alloys to cyclic deformation were evaluated through *in situ* cyclic tension to compression tests at a plastic strain amplitude of 0.02 and a constant engineering strain rate of 10^{-3} seconds^{-1} at RT and up to 533 K (260 °C). Standard fully reversed ($R = -1$), cantilever beam bending fatigue testing was performed at RT at 30 Hz on an electro-mechanical load frame using specimens designed specifically for the current study and data were plotted as nominal peak stress amplitude *vs* cycles to failure to define standard "S-N" fatigue curves. The applied load ratio was selected to be representative of crankshaft loading experienced during high power operations.[51,52] The fatigue specimen shown in Figure 1 included a notch designed to simulate a fillet adjacent to bearing journals in crank shafts; the notch has a calculated stress concentration factor (k_t) of 1.5. The nominal stress amplitude was calculated based upon peak bending stress in a cylinder of the minimum nominal diameter of the notch in Figure 1 without the effect of the stress concentration of the notch.[33] Before testing, the notch roots were polished to a 6 μm diamond finish while rotated on a lathe. A run-out condition was defined as 10^7 cycles without catastrophic failure, at which point the test was suspended. The endurance limit was determined as the maximum stress at which three specimens exhibited run-out and no failures were observed. Each test was performed at constant stress amplitude, and the number of cycles to failure was recorded. S-N data were developed by testing sample sets of typically three specimens at a given stress amplitude, and if failure occurred, the stress amplitude for the next sample set was reduced by 70 MPa. After a complete sample set achieved run-out, the stress amplitude for the last sample set was increased by 35 MPa, as compared with the first stress amplitude in which three specimens achieved run-out, to confirm the identified endurance limit.

Deep rolling was performed on a commercial horizontally opposed dual roller system[33,53] or on a special three-roller deep-rolling device (DRD) designed and constructed for this test program,[33] a schematic of which is shown in Figure 2. The roller geometry was based upon the fillet geometry shown in Figure 1 and processing equipment,[33,53] and consisted of a hardened tool steel disc with a major diameter of 80 mm and minor radius at the crown of 3.86 mm as shown in Figure 2. The roller geometry used on the commercial system had a major diameter of 108 mm with the same 3.86 mm crown radius. The two deep-rolling systems and roller geometries were demonstrated with the 4140 alloy to produce samples with equivalent results. Specifically samples were deep rolled on each system at 12.5, 15, and 17.5 kN force, and the resulting fatigue lives tested at 572 MPa bending stress amplitude were within the experimental variations in fatigue lives observed on samples processed with either rolling system.[33]

Samples were rolled at RT and at elevated temperatures (referred to as "HT"). For HT processing on the DRD, temperature was controlled with two infrared heating lamps and temperature was monitored using an exposed tip thermocouple in contact with the specimen adjacent to the fillet during the deep-rolling process. All deep rolling was conducted with 33 over-rollings, a value selected based on previous deep-rolling research[5] and common industrial practice.[2,3] RT deep rolling was performed at a rotational velocity of 200 RPM, and the HT deep rolling was performed at 13.33 RPM to reduce the applied strain rate during deep rolling.

For HT deep rolling, the indicated temperatures represent the initial sample surface temperatures at the onset of rolling. Surface temperatures were measured using exposed tip thermocouple probes, which were applied to the outer diameter of the specimen near the fillet during deep rolling. The temperature values were adjusted by use of a calibration curve which correlated surface temperatures with a spot welded thermocouple in the fillet using a trial specimen. Three starting temperatures were evaluated: 533 K, 583 K, and 613 K (260 °C, 310 °C, and 340 °C). It was found that the improvement in fatigue performance was marginal for the 533 K and 583 K (260 °C and 310 °C) starting temperatures, but for the 613 K (340 °C) starting temperature a substantial improvement in fatigue performance

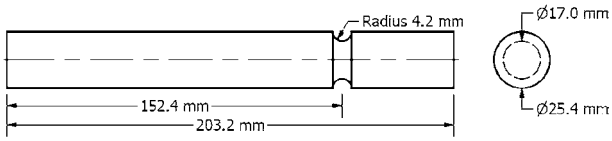

Fig. 1—Geometry of the deep-rolling bending fatigue specimen; during testing the short end was rigidly clamped.[53]

was realized for the NTB and 4140 alloy test specimens used in the trial. An additional trial was performed in which a specimen was deep rolled with an exposed tip thermocouple contacting the root of the notch during deep rolling. It was shown that during deep rolling at the 613 K (340 °C) start temperature, the fillet temperature was 588 K (315 °C) at the start of the application of peak force and due to heat loss to the rollers was reduced to 548 K (275 °C) at the end of the deep rolling process. Thus, for the HT deep-rolled data reported here, all samples were processed with an initial rolling temperature of 613 K (340 °C) at the shoulder of the fillet.

For the three-roller DRD shown schematically in Figure 2, the specimen was clamped in a three-jawed chuck which was rotated by a constant speed motor and the heating lamps would bring the specimen temperature up to the set point. The roller blocks shown in Figure 2 were connected to a hydraulic actuator and load cell, and rolling force was controlled *via* a commercial servo-hydraulic feedback control system. When the specimen set-point temperature was achieved, a load ramp sequence was initiated to apply rolling force up to the peak applied force value within two revolutions, at which point the load was maintained constant for 49.5 seconds to achieve 33 over-rolling passes and then decreased to zero within one revolution.

In order to assess the effect of applied force during deep rolling and identify a rolling force value which corresponded to the peak fatigue performance, specimens were processed in the RT and HT condition and subsequently tested to failure at a constant bending stress amplitude selected for each material and test condition. Based upon the life to failure data from each material and processing condition, a selection criterion was applied to identify a rolling load which corresponded to peak fatigue performance, and further specimens were processed for S-N fatigue analysis.

Vickers microhardness profiles were measured on untested, deep-rolled specimens which were sectioned perpendicular to the specimen axis at the minimum diameter of the notch shown in Figure 1. The specimen sections were mounted and diamond polished, and microhardness measurements were conducted along a path from the notch surface to the specimen centerline by use of a 1000 g load and a 10 seconds hold time. Complete details of the test methods including images of the experimental setup and deep-rolling systems are published elsewhere.[32,33,53]

Residual stress analysis using XRD techniques was performed on the untested fatigue samples from RT and HT deep-rolled sample sets prepared for S-N testing. All

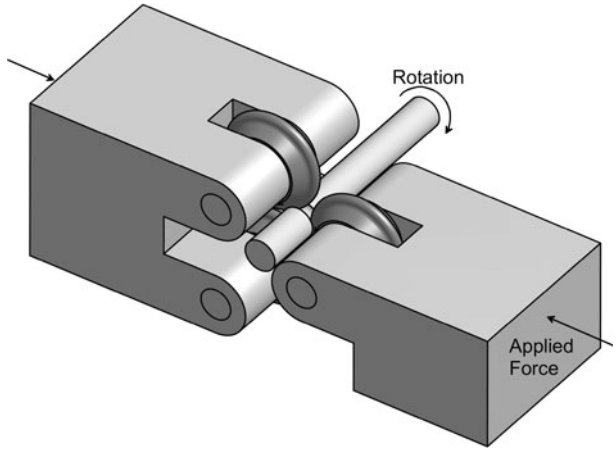

Fig. 2—Schematic of three-roller, DRD.

residual stress analyses were performed at the root of the fillet, along the axis of the sample. The shoulder of the fillet, well away from the notch root, was ground approximately 45 deg up the fillet wall to increase the available angle to the root of the notch for XRD. The stress analysis was performed according to the Δd *vs* $\sin^2\psi$ procedure outlined by Cullity.[50] XRD was performed using a chromium X-ray source with a wavelength of 2.2897 Å, with a high voltage of 35 kV and beam current of 1.5 mA using a rectangular 2 mm × 0.5 mm collimator. The (211) ferrite peak was scanned and the available 2θ ranges were from 121 to 167 deg for residual stress analysis, and the (211) peak was typically between 155 and 157 deg 2θ. In this analysis only positive ψ angles were considered and ψ varied between 0 deg and 39 to 45 deg in 3 deg increments. Peak positions were determined using a parabolic fitting function with a 20 pct bounding range to fit each peak. Reported error in the residual stress data were taken as the larger of the two values estimated from counting statistics error, and the probable error which is based upon nonlinearity in the $\Delta d/d_0$ *vs* $\sin^2\psi$ data. The residual stress, σ_ϕ, was calculated from the slope of the $\Delta d/d_0$ *vs* $\sin^2\psi$ data, m, and elastic constants according to:

$$\sigma_\phi = \frac{mE}{1+v} = \frac{m}{K} \quad \text{where } K = \frac{1+v}{E} \qquad [1]$$

where E is Young's elastic modulus, v is Poisson's ratio for the (211) crystallographic planes, and K was taken as 5.387×10^{-6} MPa^{-1}. Residual stress analysis was performed at the surface and at depths up to 0.7 mm.

III. RESULTS

A. *As-Received Microstructures and Mechanical Properties*

The as-received microstructures of the three steel alloys were examined on polished and etched metallographic samples using a scanning electron microscope.

Figure 3 shows scanning electron micrographs of the 4140 (Figure 3(a)), NTB (Figure 3(b)) and C38M (Figure 3(c)) alloys. The 4140 alloy consisted of ferrite and spheroidized carbides, where the fine ferrite grain size was a remnant of the fine martensitic lath microstructure. The NTB alloy contained elongated ferrite grains with regions of martensite and austenite (MA) aggregates, identified by the arrows in Figure 3(b). The C38M alloy microstructure was ferrite and pearlite with elongated manganese sulfide particles, a consequence of higher sulfur content added to improve machinability.

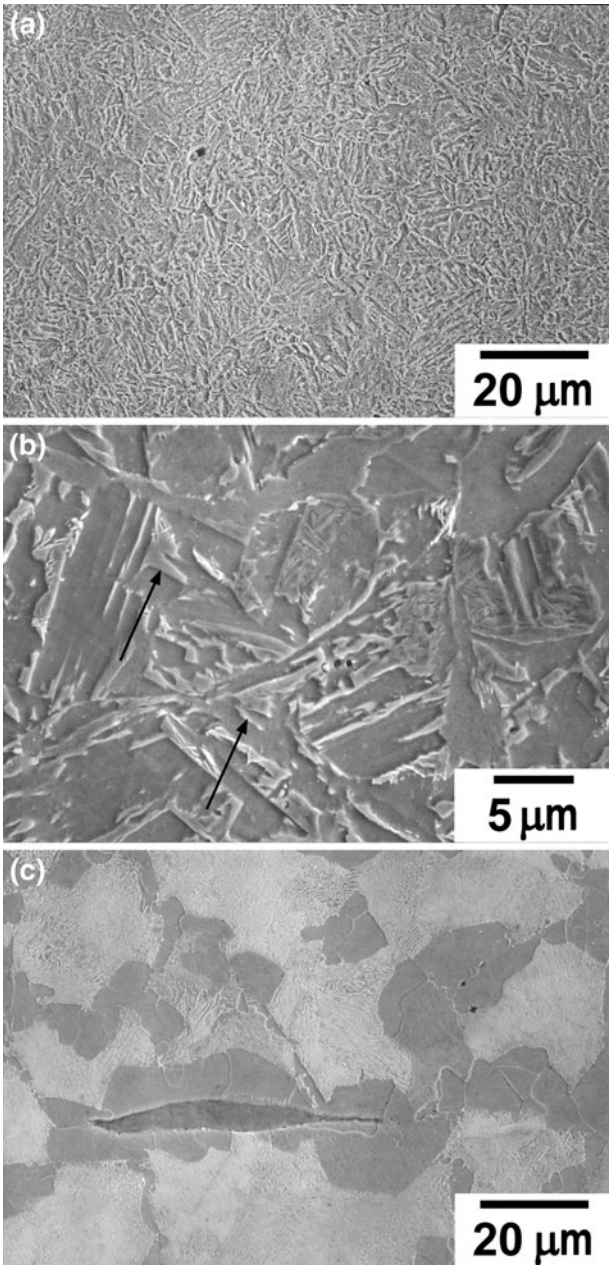

Fig. 3—Scanning electron micrographs of (*a*) 4140 Q&T steel (2 pct nital etch), (*b*) NTB steel (2 pct nital and 4 pct picral etch) and (*c*) C38M steel (2 pct nital etch), secondary electron images.[48,53] Note that the C38M image was selected to illustrate one of the sulfide inclusions present for machinability; the actual inclusion fraction is less than reflected by this image.

True stress *vs* true strain data, in both tension and compression, are shown in Figure 4 where the tensile data are plotted up to the point of instability (*i.e.*, necking). For each alloy, the results show nearly identical stress-strain behavior in compression and tension. Table II summarizes the 0.2 pct offset strain yield strengths, ultimate tensile strengths (UTS), and total elongations to failure in a 25.4-mm gage length. These data show that the 4140 alloy had the highest yield and UTS and the C38M had the lowest yield and UTS. Significant differences in initial strain hardening behavior after yielding are also apparent. At low strains the C38M and NTB steels exhibit continuous yielding and high strain hardening while the heavily tempered 4140 steel exhibits a distinct upper and lower yield point with much lower strain hardening rates (for $\varepsilon < 0.02$). All three materials exhibit similar strain hardening behavior at high strains consistent with the observation that all are ferrite-based microstructures and plastic strain decreased the effects of the initial microstructure.

B. *Effect of Temperature on Mechanical Properties*

Elevated temperature uniaxial tensile tests were performed to assess the influence of DSA on flow stress.

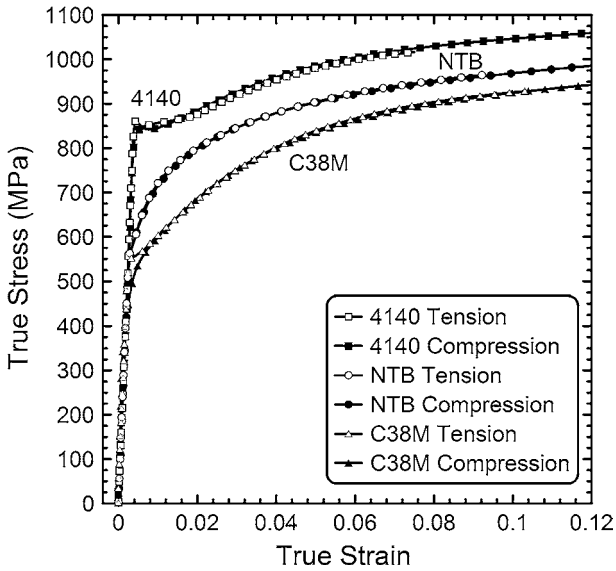

Fig. 4—Tension and compression true stress *vs* true strain relations for the 4140, NTB, and C38M steels. All tests performed at RT at an engineering strain rate ($\dot{e}$) of 1.6×10^{-3} seconds^{-1}. Adapted from Ref. [53].

Table II. As-Received RT Tensile Mechanical Property Data for the Three Steel Alloys

Steel	Eng. 0.2 Pct Yield Stress (MPa)	UTS (MPa)	Percent Strain to Failure (25.4-mm gage)
4140	848	946	21
NTB	579	881	24
C38M	552	835	20

Flow stress values at various plastic strain levels at each test temperature were determined from engineering stress *vs* engineering strain curves collected for each alloy,[33] and Figure 5 shows a representative set of data for the C38M alloy. Similar families of curves were obtained for the other two alloys.[33] The flow stress peak indicates the temperature range in which the DSA component to strengthening was maximized. For a strain rate of 10^{-4} seconds^{-1}, the temperature ranges in which DSA was effective were between 523 K and 543 K (250 °C and 270 °C) for the C38M alloy and between 473 K and 493 K (200 °C and 220 °C) for the 4140 and between 493 K and 582 K (220 °C and 309 °C) for the NTB alloys.

Single reversal Bauschinger effect tests were performed at a constant engineering strain rate of 10^{-4} seconds^{-1} *in situ* at temperatures between ambient and 634 K (361 °C) (details are provided elsewhere[33,48]). The effects of test temperature on the 0.2 pct offset strain reversed flow stress after the point of strain reversal for a tensile plastic pre-strain level of 0.02 are shown in Figure 6. The reversed flow stress data in Figure 6 exhibit an increase with an increase in test temperature, up to a plateau at approximately 533 K (260 °C) for the 4140 and C38M alloys and 582 K (309 °C) for the NTB alloy; the peaks correspond to the maximum DSA temperature for each alloy.

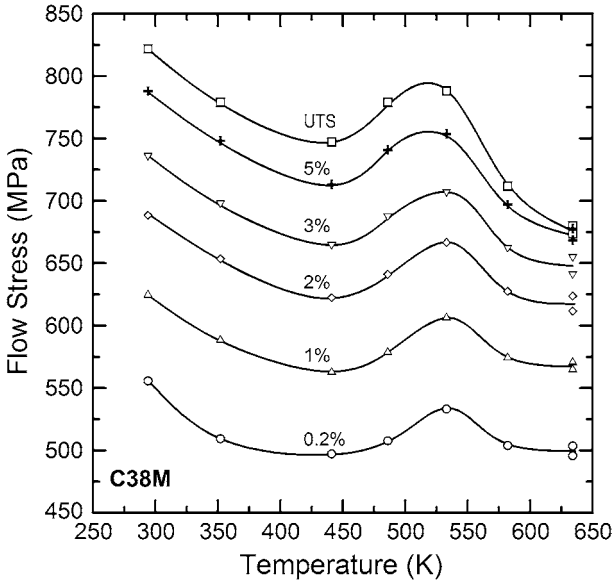

Fig. 5—Flow stress at indicated plastic strain *vs* testing temperature for C38M alloy for samples tested at a constant engineering strain rate ($\dot{e}$) of 10^{-4} s^{-1}.

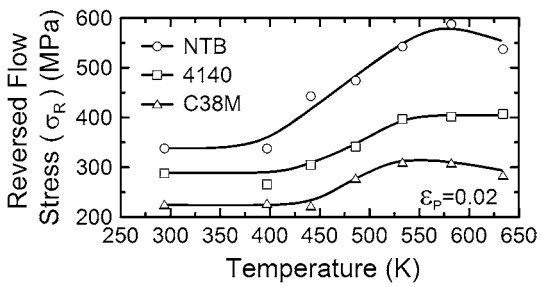

Fig. 6—The effect of temperature on reversed flow stress, σ_R, for a tensile prestrain (ε_P) of 0.02. Adapted from Ref. [48].

Based upon the improved resistance to strain reversal exhibited in the Bauschinger effect tests at 533 K (260 °C), the cyclic deformation response was evaluated for the three alloys at RT and at 533 K (260 °C). The plastic strain amplitude was maintained at $\Delta\varepsilon_P/2 = 0.02$ plastic strain at a constant engineering strain rate of 10^{-3} seconds^{-1} for up to 33 hysteresis loops. The strain rate was increased with respect to the quasi-static monotonic tests to minimize the time the load frames were exposed to HT. Figure 7 shows the peak true tensile stress formed during a given hysteresis loop *vs* the number of tensile cycles. Figure 7 shows that the NTB and C38M alloys both exhibit a moderate amount of cyclic hardening in the RT condition, and the 4140 exhibits a decrease in strength, or softening, with cyclic deformation. At the 533 K (260 °C) test temperature, the three alloys exhibit an increase in the hardening response with applied cyclic deformation, the C38M exhibits a moderate increase in hardening, the 4140 exhibits a stable hysteresis loop, and the NTB exhibits a substantial increase in the hardening response with respect to the RT behavior.

C. *Response to Deep-Rolling Processing*

Figure 8 shows the cycles to failure for specimens deep rolled at RT and HT over a range of rolling force values for the three alloys. For each condition, the applied nominal bending stress was maintained constant to isolate the effect of rolling force on fatigue resistance as measured by the cycles to failure for a given

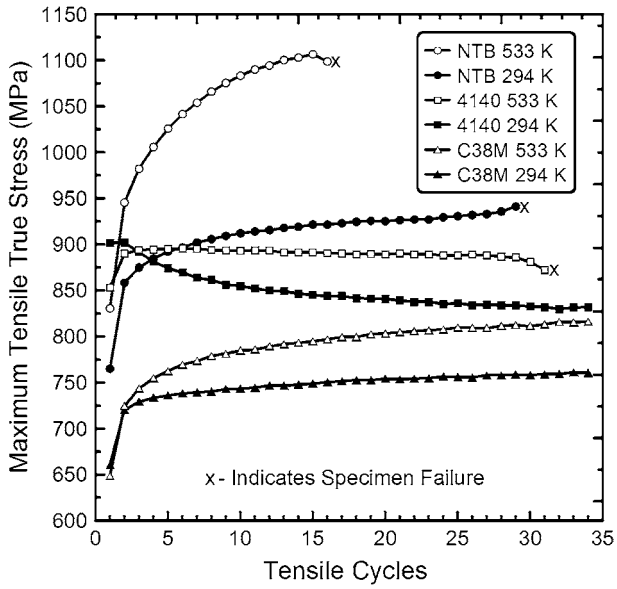

Fig. 7—Effect of temperature on the response to cyclic deformation. Shown are the maximum tensile true stress in the hysteresis loop *vs* the tensile cycle for the 4140, NTB, and C38M alloys at RT and *in situ* at 533 K (260 °C) for a plastic strain amplitude of 0.02 ($\Delta\varepsilon_P/2 = 0.02$).

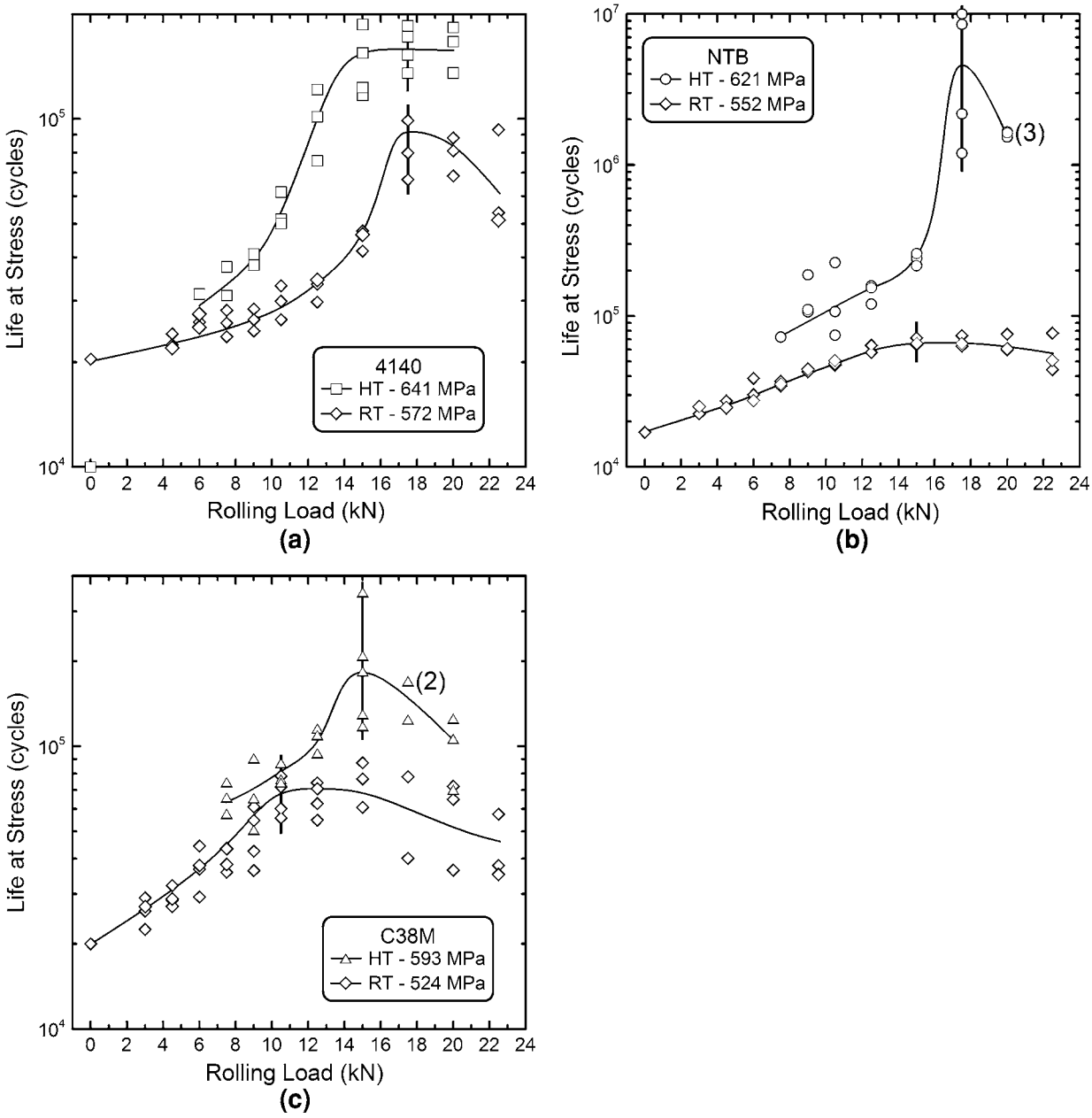

Fig. 8—Life at stress *vs* applied rolling force for the (*a*) 4140, (*b*) NTB and (*c*) C38M alloys in the RT and HT deep-rolled condition. Bending stress amplitude was maintained constant and is listed in each figure. Vertical lines represent identified rolling force values corresponding to peak fatigue performance. The number in parenthesis indicates multiple samples and the vertical lines represent the identified rolling forces values corresponding to peak fatigue performance.

processing condition. The number of over-rolling cycles was maintained constant at 33. The purpose of this study was to identify a rolling force which corresponded to the peak fatigue performance for each alloy and deep-rolling condition, and these identified rolling force values were used for further deep-rolling processing for full S-N fatigue analysis. For each alloy and deep-rolling condition, the fatigue life data exhibited an increase with an increase in applied rolling force until a peak or a plateau was achieved, further increase in applied force resulted in either a decrease in fatigue performance or an increase in the scatter of the fatigue life data, as demonstrated by the C38M RT deep-rolled data in Figure 8(c) at force levels beyond 15 kN. The deleterious effects of further increases in applied deep-rolling force on fatigue life were attributed to surface damage.[33] The selection criteria for the rolling force values corresponding to peak fatigue performance were determined as the lowest force at which samples exhibited maximum fatigue lives with minimal variability in fatigue lives, and are indicated in Figure 8 with a vertical black line.

From the data in Figure 8, the identified force values for deep rolling at RT was 17.5 kN for the 4140 alloy,

15 kN for the NTB alloy, and 10.5 kN for the C38M alloy. It is interpreted that the lower yield strengths in the NTB and C38M materials allowed for surface deformation at lower rolling loads and the gradual increase in fatigue performance with increase deep-rolling force; while the 4140 alloy, because of the higher yield strength, exhibited limited response to rolling loads below 10.5 kN. Once a sufficient force was applied to overcome the yield strength in the 4140, the fatigue performance improved substantially with small increases in rolling force.

Correspondingly as shown in Figure 8, the identified HT deep-rolling force values were determined to be 17.5 kN for the 4140 and NTB alloys, and 15 kN for the C38M alloy. Owing to the significantly enhanced fatigue performance exhibited by the HT deep-rolled samples, the selected stress amplitude was 70 MPa greater than that used for the RT deep-rolling analysis. Figure 8 shows that even with the increased bending stress amplitude, the HT deep-rolled specimens exhibit substantial increases in life for all rolling forces and exhibit a peak in performance as was observed for the RT data. The deep-rolled samples discussed in the remainder of this article were processed at the identified force values summarized in Figure 8.

The effects of deep rolling on the near-surface mechanical properties are summarized in Figure 9 which shows microhardness profiles perpendicular to the notch surface on the plane sectioning the minimum diameter of the notch from the surface to the specimen axis. The microhardness profiles in Figure 9 reflect differences in quasi-static (Figure 4) and cyclic (Figure 7) deformation behaviors between the three alloys during RT and HT deep rolling.[32,33] In the RT deep-rolled condition the NTB and C38M alloys exhibit distinct hardness peaks with an increase in hardness of 65 and 50 HV, with respect to the hardness level at the core, at depths of 0.35 and 0.25 mm, respectively. The data in Figure 4 show that the NTB and C38M alloys exhibit high strain hardening rates especially in the low strain regime and are shown to exhibit cyclic hardening under cyclic deformation at RT in Figure 7. In contrast the 4140 steel at RT exhibits no discernible change in hardness with deep rolling at RT, a high yield strength followed by negligible strain hardening as shown in Figure 4, and exhibited cyclical softening as shown in Figure 7.

In the HT deep-rolled condition all materials exhibit distinct hardness peaks with respect to the core hardness. The magnitude of the hardness peak for the 4140 steel is 85 HV at a depth of 0.4 mm, the NTB alloy exhibits a hardness increase of 135 HV at a depth of 0.35 mm, and the C38M alloy hardness increase is 100 HV at a depth of 0.3 mm. As shown in Figure 7, with an increase in temperature, the 4140 steel yield strength decreases and the cyclic response changes from softening under cyclic deformation to maintaining stable hysteresis loops. Also, the NTB and C38M alloys both exhibit an increased cyclic hardening behavior under cyclic deformation; with the NTB exhibiting a significantly higher rate of cyclic strengthening, as reflected in the microhardness data in Figures 9(b) and (c).

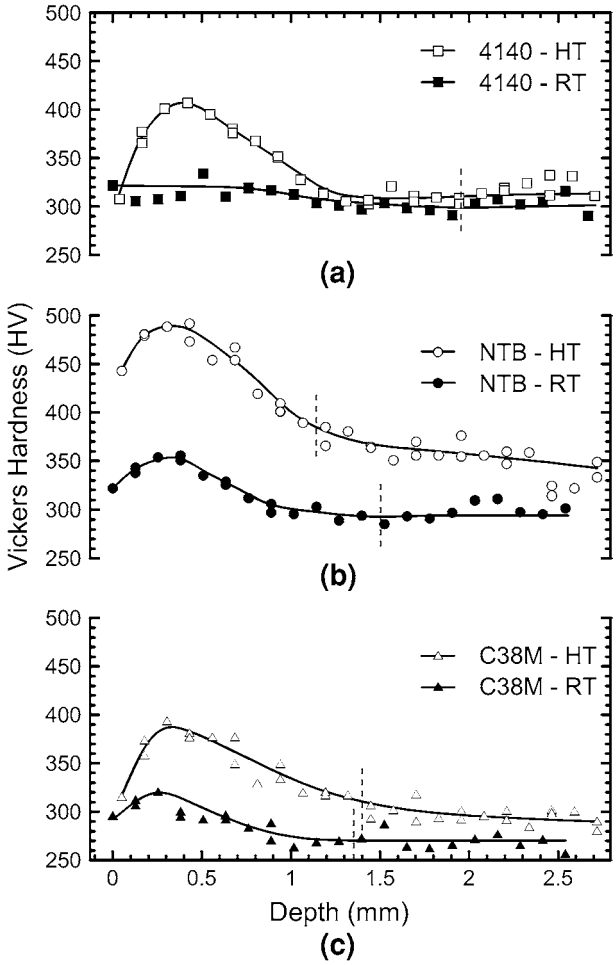

Fig. 9—Microhardness profiles for (*a*) 4140, (*b*) NTB and (*c*) C38M alloys for the RT (closed symbols) and HT (open symbols) deep rolled at the specific processing loads identified in Fig. 8. The vertical, dashed lines represent the depth of nonpropagating fatigue cracks in run-out fatigue specimens discussed below in conjunction with Fig. 12.

The effects of deep rolling at the force levels determined in Figure 8 at RT and HT for the three alloys on the axial residual stress with respect to the depth from the root of the notch are shown in Figure 10. All deep-rolling conditions produced compressive residual stresses at the notch root. Figure 10(a) shows that the RT and HT residual stress for 4140 steel specimens deep rolled at 17.5 kN rolling force are between −400 and −550 MPa and there was negligible difference between the RT and HT deep-rolling condition. Figure 10(b) shows that the HT deep-rolled NTB alloy exhibited a substantially larger magnitude residual stress in the measured depths than the RT deep-rolled condition. Figure 10(c) shows the HT deep-rolled condition exhibited similar residual stress magnitude at the surface as the RT condition, and achieved a slightly larger magnitude at depths up to 0.4 mm.

D. *Fatigue Properties*

Figure 11 shows the stress amplitude *vs* cycles to failure data, termed S-N data, for the baseline, RT deep-rolled,

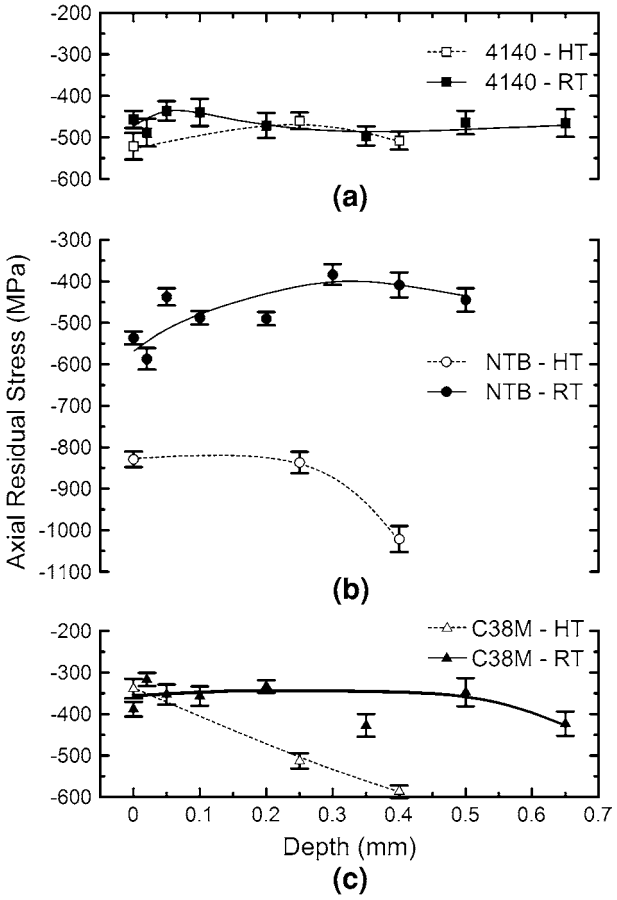

Fig. 10—Axial residual stress as measured by XRD analysis *vs* depth from the bottom of the fillet to the specimen centerline for the three alloys deep rolled at RT and elevated temperature (HT) as indicated.

and HT deep-rolled conditions for the 4140 (Figure 11(a)), NTB (Figure 11(b)) and C38M (Figure 11(c)) alloys where the deep-rolled specimen sets were processed at the rolling force values identified in Figure 8. The fatigue data exhibit excellent reproducibility at all stress levels tested and well defined endurance limits. As shown in Figure 11, in the RT deep-rolled condition, the three alloys exhibited substantial improvement in fatigue performance, especially the endurance limit, compared with the baseline behavior. The 4140, NTB, and C38M alloys exhibited RT deep-rolled endurance limits of 469, 448, and 386 MPa, respectively, which correlate to increases of 51, 62, and 60 pct over the corresponding baseline data. The finite life data for the RT deep-rolled condition all exhibited a significant improvement in the number of cycles to failure at stress amplitude levels near the endurance limit as shown in Figure 11. However, at higher stress amplitudes the finite life data converged with the baseline fatigue behavior for each alloy. It is interpreted that with an increase in bending stress amplitude, superposition of the compressive bending and residual stresses may have induced plastic deformation in the fillet thus relieving the residual stress present after deep rolling, thereby reducing the fatigue behavior to the baseline condition.

The HT deep-rolled condition exhibits a substantial improvement in fatigue strength, especially the endurance limit, compared with the RT deep-rolled condition for all alloys tested in both the finite life regimes and endurance limits. In the finite life regime the data exhibit an offset towards greater fatigue life compared with the baseline and RT deep-rolled conditions. In the HT deep-rolled condition, the nominal stress endurance limits were 607 MPa for the 4140 steel (Figure 11(a)), 586 MPa for the NTB steel (Figure 11(b)), and 524 MPa for the C38M steel (Figure 11(c)).

Table III summarizes endurance limit data and compares the effects of processing. Nominal endurance limit data tabulated are baseline (S_{BL}), RT deep rolled (S_{RT}), and HT deep rolled (S_{HT}). Also included are calculated percentage enhancements with respect to the baseline condition to assess the effect of RT and HT deep rolling, *i.e.*, RT-BL and HT-BL, respectively, as well as the extent of improvement with HT processing to RT processing (HT-RT). To compare to traditional correlations of endurance limits based on UTS, fatigue ratios that incorporate the deep-rolled sample stress concentration factor (k_t = 1.5) are also shown. These comparisons clearly indicate the degree of improvement from deep rolling, both RT and HT, and show that HT deep rolling increases the fatigue limit by approximately 100 pct with respect to the unprocessed (baseline) condition for all three alloys.

E. *Fractography*

A unique feature observed in this and other studies on fatigue in deep-rolled components[5,8,9,11,14,51,52] is the presence of arrested surface cracks in samples tested to run-out, *i.e.*, 10^7 cycles. Surface cracks were found to initiate and propagate at early stages (<500,000 cycles) during fatigue tests at stress levels defined as the endurance limit for each alloy in the RT and HT deep-rolled condition. Evidence of nonpropagating fatigue cracks included circumferential hairline rust traces along the stressed portion of the notch root due to debris ejected to the surface from the cracks. After achieving run-out, selected specimens were sectioned along the neutral plane and loaded to failure in three point bending at cryogenic temperatures to provide direct access to the crack surfaces without incurring any plastic damage during the opening process. Figure 12 shows nonpropagating fatigue crack fractographs for the three alloys in the RT and HT deep-rolled condition. The nonpropagating fatigue cracks observed in the sectioned specimens penetrated to depths between 1.15 and 1.95 mm from the surface, with a maximum depth at the location of maximum bending stress amplitude. The maximum depth values for the nonpropagating fatigue cracks in Figure 12 are indicated in the microhardness profile plots in Figure 9 by the dashed vertical lines, respectively for each alloy and deep-rolling condition. Kloos *et al.*[9] describe the phenomenon in terms of the superposition of loading and residual stresses, where during the compression portion of the fatigue cycle, imposed forces are carried by the crack face and no stress concentration occurs at the crack tip. During

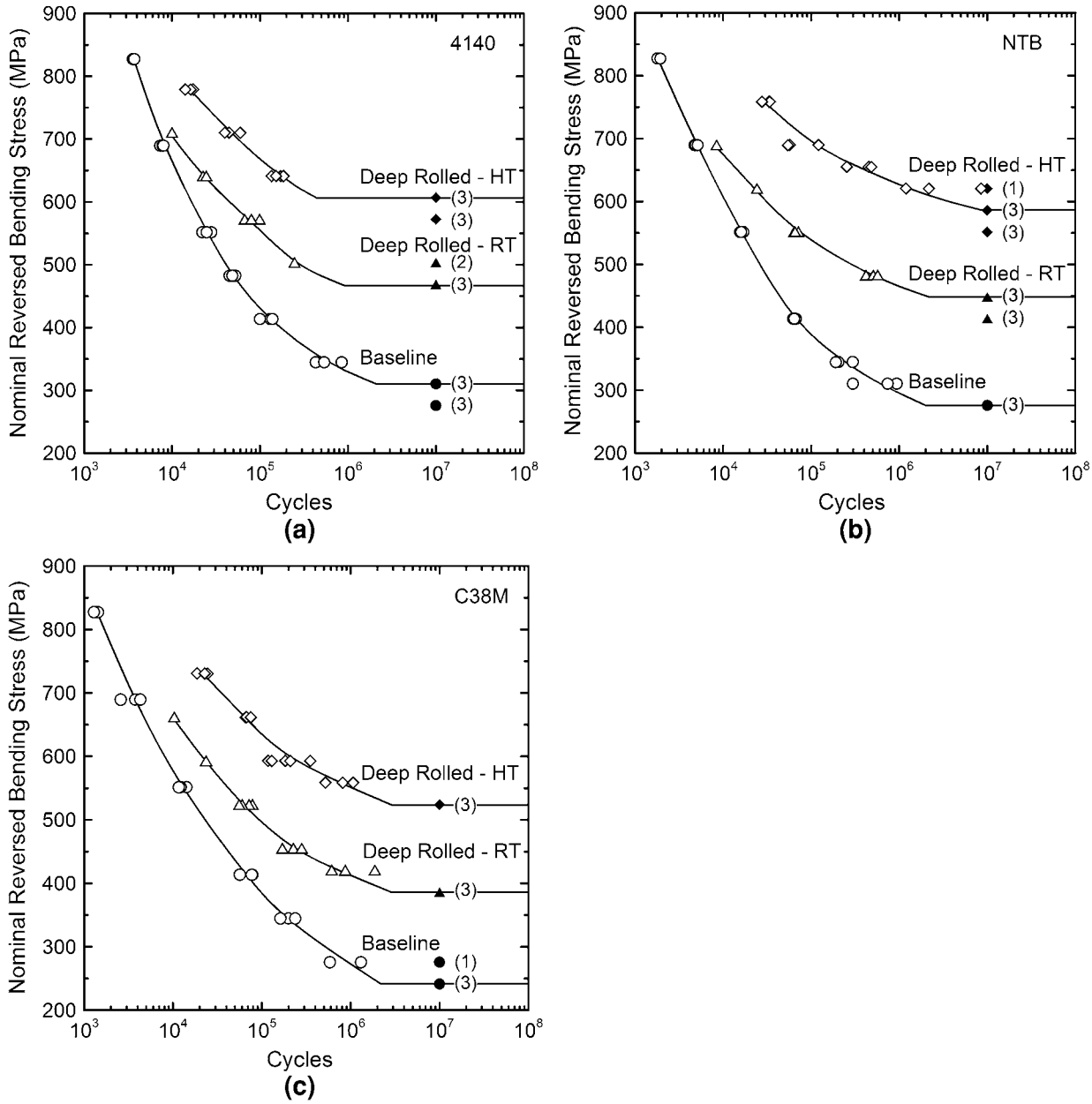

Fig. 11—RT S-N curves of the nominal reversed bending stress *vs* number of cycles to failure for the baseline (unprocessed) condition and for samples deep rolled at elevated temperature (HT) and RT at the identified HT and RT deep-rolling forces from Fig. 10 for (*a*) 4140, (*b*) NTB, and (*c*) C38M. Solid symbols represent specimens that achieved run-out, and the number in parenthesis represents multiple specimens.

the tensile phase of cyclic loading, crack arrest is believed to occur when the local stress intensity factor range at the crack tip, ΔK, falls below a threshold value, ΔK_{th}[11,14] which is influenced by both the residual and loading stresses and is discussed further below.

The fracture surfaces of all broken fatigue samples were evaluated, and selected fractographs for NTB specimens tested to failure at a nominal stress amplitude 35 MPa above the endurance limits listed in Table III are shown in Figure 13 to illustrate the general characteristics of the effects of processing history on the overall fracture behavior. The general features shown in Figure 13 are also characteristic of those observed on the other two alloys.[33] The corresponding cycles to failure for each specimen are listed in the figure caption. Each sample exhibited fatigue crack nucleation on both the top and bottom surfaces characteristic of reversed bending fatigue and some cracks exhibited ratchet marks (*e.g.*, see bottom of Figure 13(a)) indicating multiple crack nucleation sites. For the baseline condition, the fatigue crack propagated on a single plane through the cross section of the notch until the overload condition was reached and complete failure occurred. In contrast, Figures 13(b) and (c) show the fatigue fracture morphologies for the RT and HT deep-rolled conditions, respectively. The fatigue crack growth zones differ

from those shown for the baseline data and these differences are summarized in Figure 13(d), a schematic representation of the fracture surfaces of deep-rolled samples. In the deep-rolled conditions adjacent to the crack nucleation points, the fracture surfaces in the region of slow crack growth the surfaces were discolored and appeared smoother, in part due to self-polishing. The borders of the slow crack growth regions are highlighted by dotted white lines in Figures 13(b) and (c) and are the slow crack growth region identified as region "1" in Figure 13(d). Beyond the slow crack growth area a ledge exists which is indicated by white arrows in Figures 13(b) and (c), and is represented schematically in Figure 13(d). These ledges are interpreted to reflect a residual stress boundary between the deep-rolled case and undeformed core and indicate the transition from slow to more rapid fatigue crack growth in the core, the region identified as "2" in Figure 13(d). The increase in crack growth rate associated with a transition from regions 1 to 2 are clearly evident in the fracture surfaces in Figures 13(b) and (c). As the fatigue crack propagated into the tensile residual stress field in the core of the specimen, the elastically maintained compressive residual stress should decay as the cross-sectional area of material maintaining the tensile stress field is diminished *via* fatigue crack propagation. As such, the boundary between the compressive case and tensile core shifted during testing and the position of the ledge changed as indicated by the arrows in Figure 13(d). When the fatigue cracks had achieved sufficient size at the applied stress amplitude, specimen failure occurred by overload.

Table III. Comparison of the Endurance Limit Data, Change in Endurance Limit Data, and Fatigue Ratio Data for the Baseline, RT Deep-Rolled and HT Deep-Rolled Conditions

	Steel Alloy		
	4140	NTB	C38M
Fatigue property			
Nominal endurance limit (MPa)			
Baseline (S_{Bl})	310	276	241
RT deep rolled (S_{RT})	469	448	386
HT deep rolled (S_{HT})	607	586	524
Change in endurance limit (pct)			
RT-BL 100 pct * ($S_{RT} - S_{BL}$)/S_{BL}	51	62	60
HT-RT 100 pct * ($S_{HT} - S_{RT}$)/S_{RT}	29	31	36
HT-BL 100 pct * ($S_{HT} - S_{BL}$)/S_{BL}	96	112	117
Fatigue ratio			
Baseline (k_t * S_{BL}/UTS)	0.49	0.47	0.43
RT deep rolled (k_t * S_{RT}/UTS)	0.74	0.76	0.69
HT deep rolled (k_t * S_{HT}/UTS)	0.96	1.00	0.94

IV. DISCUSSION

A. *Nature of Fatigue Improvement*

Deep rolling is a processing method which addresses three primary approaches to enhancing fatigue performance: inhibition of fatigue crack initiation through improvement of surface finish by burnishing during deep rolling; increase in surface strength *via* work hardening; and a reduction in the effective surface cyclic tensile stress through the introduction of compressive residual stress.[2,15] Of these, the development of an effective residual stress distribution is usually identified as the primary factor which improves fatigue resistance.[9,13,15] The results in Figure 11 and Table III show that deep rolling provides a substantial improvement in fatigue performance in the three alloys tested, providing

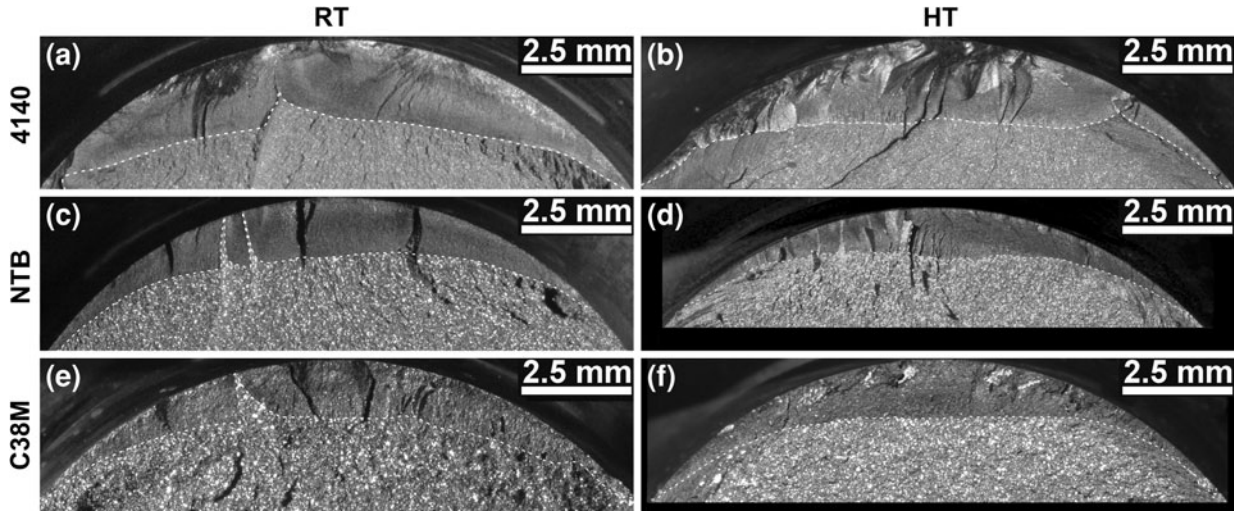

Fig. 12—Light optical fractographs of nonpropagating cracks in run-out specimens, deep rolled at RT and elevated temperature (HT) as indicated for the (*a*, *b*) 4140, (*c*, *d*) NTB and (*e*, *f*) C38M alloys. The samples were deep rolled at the force levels identified in Fig. 8 and tested at the endurance limits listed in Table III. The dark surface corresponds to fatigue cracks which formed within approximately 500,000 cycles but did not result in catastrophic failure after 10^7 cycles, and the bright surface is the fracture surface created during the process to open the fatigue crack at cryogenic temperatures to minimize plastic deformation. A dashed white line was introduced to demark these two fracture surface features.

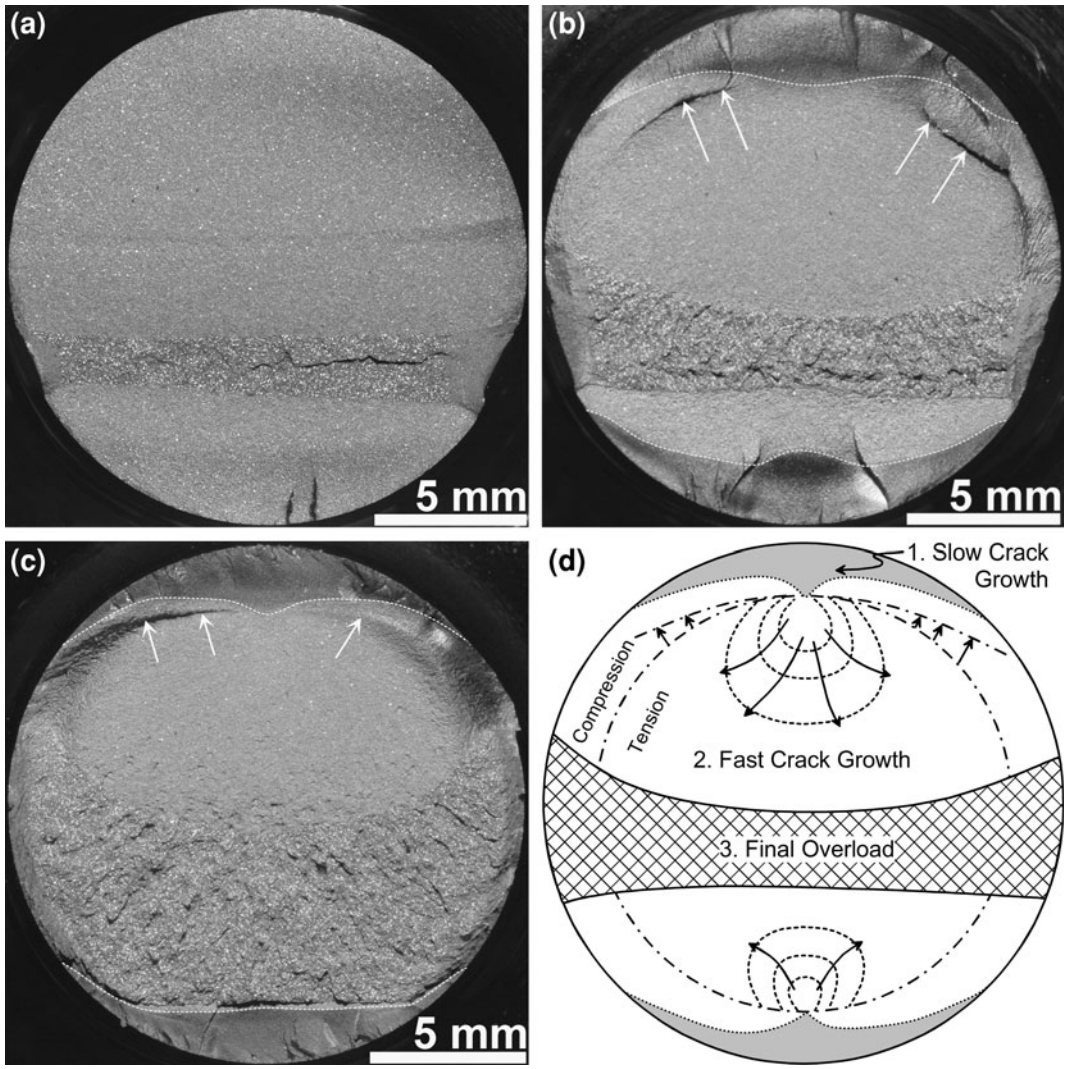

Fig. 13—Fractographs of NTB alloy fatigue specimens tested at a nominal stress amplitude 35 MPa above the reported endurance limits from Table III for the (*a*) baseline, (*b*) RT deep-rolled, (*c*) HT deep-rolled condition NTB alloy and (*d*) schematic of crack propagation in deep-rolled specimens. Measured cycles to failure values were 990,830 cycles for the baseline condition in (a), 507,588 cycles for the RT deep-rolled condition in (b) and 8,526,094 cycles for the HT deep-rolled condition in (c).

between 51 and 62 pct increase in the endurance limit for the RT deep-rolled condition and 96 to 117 pct for the HT deep-rolled condition compared with the baseline fatigue behavior.

The effect of burnishing of the notch surface during deep rolling is primarily an effect of an inhibition of fatigue crack initiation due to an improvement of notch surface finish. The effect of burnishing on the improvement in fatigue performance due to inhibition of crack initiation between the RT and HT deep-rolled conditions as compared with the baseline condition should be minimal because all specimens were polished before testing for the baseline condition and before rolling for the RT and HT deep-rolled conditions. Burnishing has negligible impact on fatigue crack propagation or arrest as in the case of the nonpropagating fatigue cracks shown in Figure 12. As surface cracks were consistently observed in RT and HT deep-rolled endurance limit specimens the effect of burnishing on the enhancement of measured endurance limits by deep rolling was interpreted to be negligible.

The importance of surface strength and residual stress on the enhancement of endurance limits by deep rolling in the present research is demonstrated by considering the schematic drawing in Figure 14, which shows the cross section of the notch of a deep-rolled fatigue specimen as observed with symmetric, nonpropagating fatigue cracks similar to those presented in Figure 12. The horizontal dashed lines in Figure 14 represent the surface and crack arrest depth along line A-B at the point of maximum bending stress amplitude and crack depth. A schematic representation of the residual stress profile to the left of the schematic is based on data from Figure 10 and schematic representation of two microhardness profiles to the right are based upon data from Figure 9. The two microhardness profiles in Figure 14

represent the extremes of the microhardness data in Figure 9 and indicate profiles for the RT deep-rolled 4140 and HT deep-rolled NTB alloys. As shown in Figure 9 the microhardness peaks occur at depths up to 0.4 mm for the three alloys in the two deep-rolling conditions and the transition between the hardened layer and the core occurs at depths of between 0.9 and 1.4 mm. Due to the presence of the nonpropagating fatigue cracks in the endurance limit fatigue tests in which the cracks extend beyond the hardened layer (1.15-1.95 mm) as shown in Figure 12, where the depth of the nonpropagating fatigue crack is indicated on the microhardness profile in Figure 9, it is interpreted that the increased strength due to work hardening associated with deep rolling has a secondary effect on measured endurance limits.

The residual stress profile in Figure 14 approximates the shape of the measured data shown in Figure 10 for the 4140 alloy in the RT and HT deep-rolled condition, which shows that compressive residual stresses were essentially constant to a depth of 0.65 mm.[33] The axial residual stress in Figure 14 is assumed to become tensile at a depth corresponding to the maximum penetration of plastic deformation of deep rolling. Based upon the observations of nonpropagating fatigue cracks at the endurance limits, and the discussion of the negligible contributions of burnishing and surface work hardening to measured endurance limits, it is concluded that the improvements in endurance limits by deep rolling the alloys studied here primarily reflect the effects of compressive residual stresses, which are interpreted to extend beyond the crack arrest depth as indicated in the schematic in Figure 14. It should be noted that the effect of burnishing and increased surface hardness represent potentially significant sources of endurance limit improvement not reflected in the endurance limit gains demonstrated in the present research.

The data in Figure 14 and Table III show that deep rolling at HT provides a substantial additional improvement in fatigue performance over that observed by RT deep rolling. Specifically, deep rolling at DSA temperatures provides a 29-36 pct improvement in fatigue performance as compared with the RT deep-rolled condition. In ferritic materials subjected to strain reversals, DSA substantially increases the resistance to strain reversal,[48] as shown in Figure 6. The presence of nonpropagating fatigue cracks in run-out fatigue specimens tested at the endurance limit indicates that the increases in endurance limits in the RT and HT deep-rolled conditions are due to the presence of compressive residual stresses. These findings suggest that the improvement in fatigue performance with HT processing is due to the improved stability of residual stresses during cyclic loading. The improved stability results from the increased resistance to strain reversal of the material in the deformation volume as a consequence of the effects of deep rolling at DSA temperatures on the dislocation substructure generated during deformation. These findings are consistent with those for HT deep-rolled SAE 1045[38–40] and HT shot-peened AISI 4140.[36,37] Direct observations of dislocation structure changes due to HT deep rolling, and their direct relationship to residual stress profiles should be the subject of future HT deep-rolling studies as these data will be necessary to provide guidance to alloy development and processing strategies to further optimize the enhancement of fatigue performance in deep-rolled components.

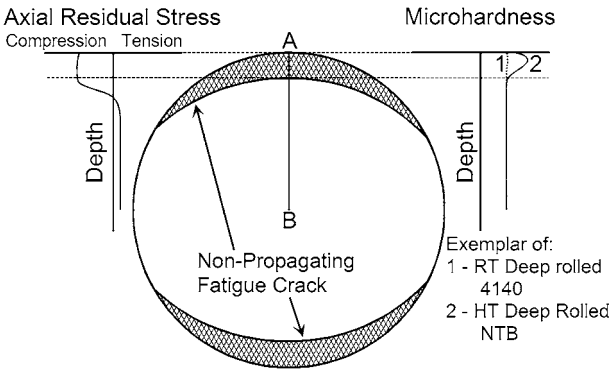

Fig. 14—Schematic of notch cross section of deep-rolled fatigue specimen showing nonpropagating fatigue cracks symmetric about the neutral axis with schematic representations of microhardness profiles of the RT deep-rolled 4140 alloy (dashed line number 1) and HT deep-rolled NTB alloy (solid line number 2) along with anticipated axial residual stress component profile generated through deep-rolling processing along line A-B.

B. *Comparison with Quasi-Static Mechanical Properties*

Figure 15 correlates the nominal measured endurance limits with the as-received RT tensile strengths for the baseline, RT deep-rolled, and HT deep-rolled conditions for the three alloys. The data in Figure 15 show that the nominal endurance limits linearly correlate to UTS, and the linear correlation shifts to higher endurance limits

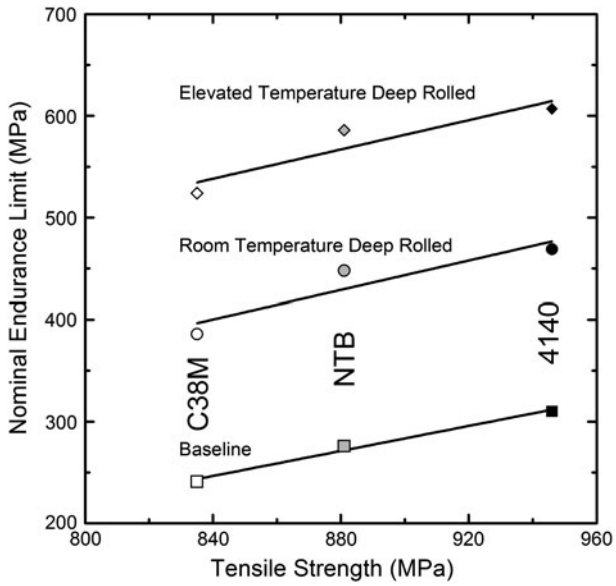

Fig. 15—Nominal endurance limit *vs* UTS at RT for the baseline, RT deep-rolled, and HT deep-rolled condition for the three alloys, 4140 (closed symbols), NTB (gray symbols), and C38M (open symbols).

with RT and HT deep rolling. To compare directly with previous research, the nominal endurance limits are multiplied by the stress concentration factor for the notch in the experimental sample (*i.e.*, $k_t \times S_f$) and are re-plotted in Figure 16. Also included in Figure 16 are the published data on a German steel grade 37 CrS 4[9] and a series of reference lines for fatigue ratios (ratio of the endurance limit to UTS) from 0.4 to 1.0. Figure 16 shows that the baseline fatigue behavior for the steels evaluated here plot between the lines for fatigue ratios of 0.4 and 0.5 as would be expected for highly polished wrought steel.[54] The RT deep-rolled fatigue ratios for the three alloys used in the current study ranged between 0.69 and 0.76, which is slightly higher than the RT deep-rolled condition for the 37 CrS 4 data from Kloos *et al.*[9] which was approximately 0.6 over the range of tensile strengths evaluated. Kloos *et al.*[9] were not specific as to whether the reported endurance limit values included the stress concentration effect. The HT deep-rolled conditions demonstrated a fatigue ratio between 0.94 and 1.00, which is a significant increase as compared with the RT deep-rolled condition.

The importance of direct measurement of the resistance to flow during reversed loading, as observed in Bauschinger effect tests, to the characterization of materials processed by RT and HT deep rolling is illustrated in Figure 17 which correlates RT and HT deep-rolling nominal endurance limit data with reversed flow stress data after a 0.02 pre-strain presented in Figure 5.[33,48] The reversed flow stress data were obtained from Bauschinger effect tests at RT, 533 K, and 582 K (260 °C and 309 °C, respectively) for the 4140, NTB, and C38M alloys. The data from the Bauschinger effect tests at both 533 K and 582 K (260 °C and 309 °C, respectively) are presented here because the average temperature values experienced during HT deep rolling occurred within this temperature range.[33] The data in Figure 17 show that for the three materials considered here, measured nominal endurance limits increase with reversed yield stress. However, while the data for the ferrite plus carbide microstructures (*i.e.*, C38M and 4140 steels) exhibit similar slopes that would characterize a single property band, the data for the NTB alloy, which had a microstructure consisting of ferrite, martensite, and retained austenite, exhibit a significantly lower sensitivity to reversed flow stress. This difference is interpreted[33] to reflect the effects of austenite transformation with deformation[55] and the corresponding effect of this transformation on the depression of measured endurance limits. An example of one such mechanism would be the reduction of compressive surface residual stresses during cyclic loading due to the strain associated with stress induced austenite to martensite transformation in the undeformed core of the specimen which is under tensile residual stress. This mechanism would be unrelated to the resistance to strain reversal of the material, but would decrease the effective slope of the data in Figure 17 and warrants additional research. However, the general trend shown in Figure 17 is that the fatigue strength increase with an increase in reversed flow strength, which is a measure of the resistance to strain reversal.

The results of this study provide direct evidence of the importance of controlling microstructure and processing conditions required to maximize the fatigue performance in medium carbon forging steels. Future studies will be required to directly assess the effects of deep rolling, and variations in rolling temperature, on microstructural changes and residual stress profiles within the process zone affected by the rolling process. Also,

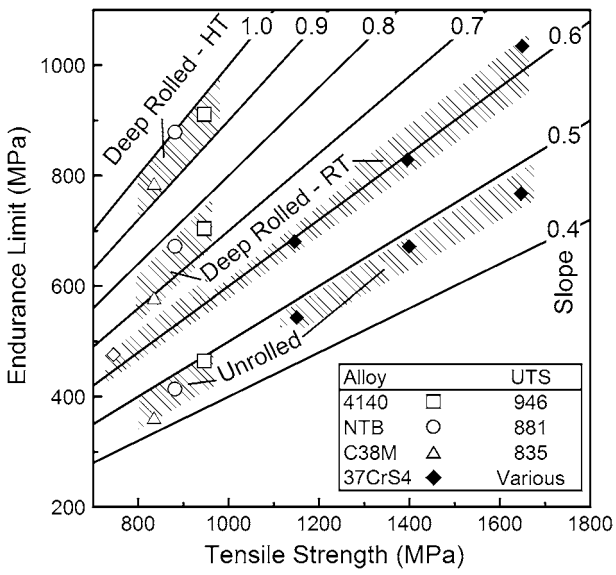

Fig. 16—Endurance limit *vs* UTS at RT for the baseline, RT deep-rolled, and HT deep-rolled condition for the three alloys used in the current study where the endurance limit values are adjusted by the stress concentration factor and German steel grade 37 CrS 4 re-plotted from Ref. [9].

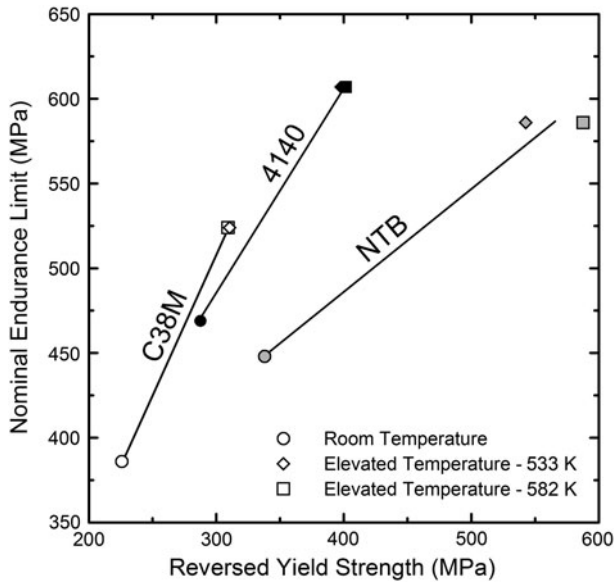

Fig. 17—Nominal endurance limit *vs* reversed flow stress (σ_R) at 0.02 pre-strain for 4140 (closed symbols), NTB (grey symbols), and C38M (open symbols) deep rolled at RT and HT. The legend indicates the temperature at which the reversed yield strength data were measured.

further analysis of the potential use of measurements from nonstandard mechanical tests, such as the reversed flow stress measurements discussed in Figure 17, to assess the applicability of selected alloy content modifications and microstructural changes to produce materials that would respond more effectively to RT and HT deep rolling, and thus produce components with enhanced performance, is required.

V. CONCLUSIONS

(1) Deep rolling significantly enhances the fatigue resistance of the three medium carbon bar steels, a quenched and tempered 4140, a direct-cooled NTB steel with retained austenite, and a microalloyed ferrite-pearlite steel, as measured by means of a specially developed laboratory test method that exhibited excellent reproducibility.
(2) Deep rolling at temperatures within the DSA range for each alloy results in further increases in room temperature fatigue performance in comparison to the same materials deep rolled at room temperature. The additional increase was interpreted to reflect residual stress fields stabilized against mechanically induced relaxation during cyclic loading as quantified *via* enhanced resistance to strain reversal in Bauschinger effect tests.
(3) The significant enhancement to measured endurance limits provided by RT and HT deep-rolling processing was determined to result primarily from the introduction of beneficial compressive residual stresses in the fillet of the specimen. The contribution of surface burnishing was determined to be negligible because of the presence of nonpropagating surface fatigue cracks in endurance limit specimens, as burnishing has no effect on crack propagation or arrest. The contribution of work hardening in the deformed surface layer was determined to be negligible as the arrest depth of the nonpropagating fatigue cracks in the endurance limit specimens extended beyond the hardened layer as determined through microhardness profile analysis.
(4) The endurance limit values for the baseline, RT deep-rolled, and HT deep-rolled conditions scale with the as-received room temperature UTS.
(5) The endurance limits of deep-rolled samples scale directly with measurements of the resistance to reversed flow in Bauschinger effect tests, both at room temperature and elevated temperatures.

ACKNOWLEDGMENTS

The authors gratefully acknowledge the support of the sponsors of the Advanced Steel Processing and Products Research Center, an industry/university cooperative research center at the Colorado School of Mines.

REFERENCES

1. "The World's Top 10 Best Engines Use Steel: Analysis of Ward's AutoWorld Top 10 Best Engine List for 2004," American Iron and Steel Institute, Retrieved Feb. 12, 2008, from www.autosteel.org.
2. H. Naumann: *Deep Rolling of Highly Stressed Components*, American Society of Tool and Manufacturing Engineers, Technical Paper no. MF68-169, 1968, pp. 1–7.
3. E. Randlett: *Deep Rolling of Crankshaft*, Society of Manufacturing Engineers (SME), Material Forming Report no. MF70-262, 1970.
4. H.J. Naumann: *Metalworking*, 1968, vol. 24 (2), pp. 48–50.
5. K.H. Kloos, B. Fuchsbauer, and J. Adelmann: *Int. J. Fatigue*, 1987, vol. 9, pp. 35–42.
6. G.N.J. Gilbert and K.B. Palmer: *The Influence of Surface Rolling on the Fatigue Properties of Flake Graphite and Nodular Graphite Cast Irons*, British Cast Iron Research Association (B.C.I.R.A.) Research Report No. 392, 1954, pp. 447–64.
7. E. Broszeit, H. Steindorf, and G. Schlieper: in *Proceedings of the 1986 International Powder Metallurgy Conference*, Verlag Schmid, Dusseldorf, FRG, 1986, pp. 403–06.
8. K.H. Kloos, E. Broszeit, B. Fuchsbauer, and F. Schmidt: *Zeitschrift Fur Werkstofftechnik*, 1981, vol. 12, pp. 359–65.
9. K.H. Kloos and J. Adelmann: *J. Mech. Behav. Mater. (U.K.)*, 1989, vol. 2, pp. 75–86.
10. B. Fuchsbauer: Dr.-Ing. Dissertation, Von dem Fachbereich Maschinenbau an der Technischen Hochschule Darmstadt, 1983.
11. A. Drechsler, T. Dörr, and L. Wagner: *Mater. Sci. Eng. A*, 1998, vol. 243, pp. 217–20.
12. L. Wagner: *Mater. Sci. Eng. A*, 1999, vol. 263, pp. 210–16.
13. T. Watmough and M.J. Malatesta: *Trans. Am. Foundrymen's Soc.*, 1984, vol. 92, pp. 83–99.
14. F. Galzy, H. Michaud, and J.M. Sprauel: *Mater. Sci. Forum*, 2005, vols. 490–491, pp. 384–89.
15. G.E. Dieter: *Mechanical Metallurgy*, 3rd ed., McGraw-Hill, New York, 1986, pp. 408–12.
16. J. Bauschinger: *Civilingenieur*, 1881, vol. 27, pp. 289–348.
17. L. Zhonghua and G. Haicheng: *Metall. Trans. A*, 1990, vol. 21A, pp. 717–24.
18. R.C. Daniel and G.T. Horne: *Metall. Trans.*, 1971, vol. 2, pp. 1161–72.
19. A. Aran and M. Demirkol: *Mater. Sci. Eng.*, 1981, vol. 47, pp. 89–92.
20. A. Goel, R.K. Ray, and G.S. Murty: *Scripta Metall.*, 1983, vol. 17, pp. 375–80.
21. R.E. Stoltz and R.M. Pelloux: *Metall. Trans. A*, 1976, vol. 7A, pp. 1295–1306.
22. Y.M. Yaman, A. Özsoy, and K. Taşci: *J. Mater. Sci. Lett.*, 1990, vol. 9, pp. 429–31.
23. R.E. Stoltz and R.M. Pelloux: *Scripa Metall.*, 1974, vol. 8, pp. 269–76.
24. D.V. Wilson and P.S. Bate: *Acta Metall.*, 1986, vol. 34 (6), pp. 1107–20.
25. P.B. Prangnell, T. Downes, P.J. Withers, and T. Lorentzen: *Mater. Sci. Eng. A*, 1995, vol. 197, pp. 215–21.
26. J.D. Embury: in *Strengthening Methods in Crystals*, A. Kelly and R.B. Nicholson, ed., Halstead Press, New York, 1971, pp. 331–402.
27. A. Abel and R.K. Ham: *Acta Metall.*, 1966, vol. 14, pp. 1489–94.
28. D.V. Wilson: *Acta Metall.*, 1965, vol. 13, pp. 807–14.
29. J.C. Fisher, E.W. Hart, and R.H. Pry: *Acta Metall.*, 1953, vol. 1, pp. 336–39.
30. E. Orowan: in *Internal Stresses and Fatigue in Metals*, G.M. Rassweiler and W.L. Grube, ed., Elsevier, London, 1959.
31. A. Plumtree and H.A. Abdel-Raouf: *Int. J. Fatigue*, 2001, vol. 23, pp. 799–805.
32. D.K. Matlock, M.D. Richards, and J.G. Speer: *Mater. Sci. Forum*, 2010, vols. 638–642, pp. 142–47.
33. M.D. Richards: Ph.D. Thesis, No. T-6595, Colorado School of Mines, Golden, 2008.
34. A. Zeren and M. Zeren: *J. Mater. Process. Technol.*, 2003, vol. 141, pp. 86–92.
35. D.J. Dingley and D. McLean: *Acta Metall.*, 1967, vol. 15, pp. 885–901.
36. A. Wick, V. Schulze, and O. Vöhringer: *Mater. Sci. Eng. A*, 2000, vol. A293, pp. 191–97.

37. R. Menig, V. Shulze, and O. Vöhringer: *Mater. Sci. Eng. A*, 2002, vol. A335, pp. 198–206.
38. P. Juijerm and I. Altenberger: *J. Met. Mater. Miner.*, 2007, vol. 17, pp. 37–41.
39. I. Altenberger, I. Nikitin, and B. Scholtes: in *Proceedings of the 9th International Conference of Shot Peening*, V. Schulze and A. Kiku-Lari, ed., IITI International, Paris, France, 6–9 September 2005, pp. 253–60.
40. I. Altenberger: in *Proceedings of the 9th International Conference of Shot Peening*, V. Schulze and A. Kiku-Lari, ed., IITI International, Paris, France, 6–9 September 2005, pp. 144–55.
41. I. Nikitin, I. Altenberger, and B. Scholtes: in *Proceedings of the 9th International Conference of Shot Peening*, V. Schulze and A. Kiku-Lari, ed., IITI International, Paris, France, 6–9 September 2005, pp. 185–90.
42. P. Juijerm and I. Altenberger: *Scripta Mater.*, 2007, vol. 56, pp. 285–88.
43. W.C. Leslie: *The Physical Metallurgy of Steels*, 3rd ed., McGraw-Hill, New York, 1981, p. 91.
44. J.W. Edington and R.E. Smallman: *Acta Metall.*, 1964, vol. 12, pp. 1313–28.
45. J.G. Morris: *Mater. Sci. Eng.*, 1974, vol. 13, pp. 101–08.
46. S. Okamoto, D.K. Matlock, and G. Krauss: *Scripta Metall. Mater.*, 1991, vol. 25, pp. 39–44.
47. C.-C. Li, J.D. Flasck, J.A. Yaker, and W.C. Leslie: *Metall. Trans. A*, 1978, vol. 9A, pp. 85–89.
48. M.D. Richards, C.J. Van Tyne, and D.K. Matlock: *Mater. Sci. Eng. A*, 2011, vol. 528, pp. 7926–32.
49. D.K. Matlock, G. Krauss, and J.G. Speer: *J. Mater. Process. Technol.*, 2001, vol. 117, pp. 324–28.
50. B.B. Cullity: *Elements of X-Ray Diffraction*, 2nd ed., Addison-Wesley Publishing Co, Reading, 1978, pp. 411–15, 447–69.
51. R.J. Love and D.N. Waistall: "The Improvement in the Bending Fatigue Strength of Production Crankshafts by Cold Rolling," Motor Industry Research Association (MIRA) Report No. 1954/2, Nov. 1954.
52. H. Michuad, J.M. Sprauel, and F. Galzy: *Mater. Sci. Forum*, 2006, vols. 524–525, pp. 45–49.
53. M.D. Richards, D.K. Matlock, and J.G. Speer: *SAE Technical Publication #2004-01-1528*, SAE, Warrendale, 2004.
54. H.O. Fuchs and R.I. Stephens: *Metal Fatigue in Engineering*, John Wiley & Sons, New York, 1980, p. 69.
55. G.B. Olson: in *Deformation Processing and Structure*, G. Krauss, ed., American Society for Metals, Metals Park, 1984, pp. 391–424.